Invited Paper

Anisotropic multi-resolution analysis in 2D, Application to long-range correlations in cloud mm-radar fields

Anthony B. Davis*[a], Alexander Marshak[b], and Eugene Clothiaux[c]

[a]Los Alamos National Laboratory, Space & Remote Sensing Science Group, Los Alamos, NM 87545.

[b]NASA's Goddard Space Flight Center, Climate & Radiation Branch, Greenbelt, Md 20771.

[c]The Pennsylvania State University, Department of Meteorology, University Park, Pa 16802.

ABSTRACT

Taking a wavelet standpoint, we survey on the one hand various approaches to multifractal analysis, as a means of characterizing long-range correlations in data, and on the other hand various ways of statistically measuring anisotropy in 2D fields. In both instances, we present new and related techniques: (*i*) a simple multifractal analysis methodology based on Discrete Wavelet Transforms (DWTs), and (*ii*) a specific DWT adapted to strongly anisotropic fields sampled on rectangular grids with large aspect ratios. This DWT uses a tensor product of the standard dyadic Haar basis (dividing ratio 2) and a non-standard triadic counterpart (dividing ratio 3) which includes the famous "French top-hat" wavelet. The new DWT is amenable to an anisotropic version of Multi-Resolution Analysis (MRA) in image processing where the natural support of the field is 2^n pixels (vertically) by 3^n pixels (horizontally), n being the number of levels in the MRA. The complete 2D basis has one scaling function and five wavelets. The new MRA is used in synthesis mode to generate random multifractal fields that mimic quite realistically the structure and distribution of boundary-layer clouds even though only a few parameters are used to control statistically the wavelet coefficients of the liquid water density field.

Keywords: 2D multi-resolution analysis, wavelet transforms, statistical anisotropy, long-range correlations, scale-invariance, multifractal analysis, random cascade models, "$1/f$" noises, clouds, mm-radar.

1. INTRODUCTION

Anisotropy occurs in a wide variety of physical, chemical and biological systems ranging from quasi-crystalline condensed matter to the large-scale structure of the universe. The authors' special interest is in cloud structure, as defined by the liquid water density field; because of its gravity, Earth's atmosphere is strongly anisotropic with respect to the vertical (cloud layers); the effect of topography and Coriolis forces on wind patterns also causes a more subtle form of anisotropy in the horizontal plane (fronts, waves and cyclonic patterns). This underscores the need for analysis tools that can detect and quantify robust statistical anisotropy in 2D data, geophysical or other.

In geophysical data analysis at large, and data pertaining to cloud structure in particular, it is important to bear in mind that spatial correlations can be very long-range. Often the variability is strongly intermittent as well, i.e., bursts of high-frequency activity that are not amenable to Gaussian statistics. Both issues can be addressed simultaneously in the framework of multifractal analysis that has proven valuable in a wide variety of applications ranging from chaos theory and turbulence (where it was first conceived) to high-energy particle physics and cosmology. The hallmark of multifractal analysis is power-law spatial statistics of all orders, over a broad range of scales.

Wavelet theory is well-suited to describe multi-scale phenomena, with arbitrary intensity and degree of localization. In particular, wavelet transforms (WTs) and multifractal formalism are enjoying a natural and prosperous marriage[1]. However, wavelet-multifractal analyses of data have been almost exclusively based on the Continuous WT (CWT) to date. In the present study, we rectify this unnecessary neglect of simpler Discrete WTs (DWTs) which benefit from the computational efficiency of Multi-Resolution Analysis (MRA). Building on DWT and MRA theories, we also make headway into the problem of characterizing anisotropy in 2D settings.

The paper is outlined as follows. In the next section, we survey wavelet-assisted multifractal data analysis in 1D and illustrate new DWT-based methods with data describing horizontal cloud structure. Section 3 is devoted to 2D issues: How to treat data that is statistically isotropic? What are our options in highly anisotropic situations? A new DWT/MRA approach to anisotropy is presented. Our motivation for relaxing the all-too-standard assumption of isotropy is again rooted in atmospheric processes: cloud formation and maintenance in presence of strong stratification. In section 4, we summarize our results. In an appendix, we recast documented procedures for generating a representative selection of scale-invariant

* Correspondence: Email: adavis@lanl.gov; WWW: http://nis-www.lanl.gov/~adavis; Tel/Fax: (505) 665 6577/667 3815.

stochastic models in discretized wavelet space. Some models are well-known additive constructs (namely, fractional Brownian motions) but these are monofractal; others are less-known and strongly multifractal (multiplicative cascades, bounded or singular), and we shed some new light on their connection via the nonlinear transformation of exponentiation.

2. WAVELETS AND MULTIFRACTAL DATA ANALYSIS IN ONE DIMENSION

2.1. Useful wavelet definitions

We assume in the following that the 1D data

$$f(x),\ 0 \le x < L_f, \tag{1}$$

is given on a regular grid with constant $\ell = 1$; there can be several f's in an ensemble of interest, possibly of unequal lengths.

2.1.1. Continuous wavelet transform

Assuming $\psi(x)$ is a real admissible (zero-mean, at least once-oscillating) wavelet, we define the CWT of $f(\cdot)$ as

$$T_\psi[f](a,b) = \frac{1}{a}\int f(x)\psi\left(\frac{x-b}{a}\right)\,dx, \tag{2a}$$

where

$$\begin{cases} 0 < a \le L = \min_f\{L_f\} \\ 0 \le b < L \end{cases}, \tag{2b}$$

assuming periodic extension in both directions; we can define a similar integral transform $T_\varphi[f](a,b)$ for the scaling function $\varphi(x)$, which is essentially a "wavelet" with none rather than one or more oscillations. In practical computations, the pair (a,b) has discrete values (often integers, in pixel-units). Notice we use an "L_1" normalization in Eq. (2a), rather than the more standard "L_2" normalization (where a factor $a^{-1/2}$ appears).

Examples based on the Gaussian curve are:

$$\varphi_G(x) = \exp[-x^2/2]/\sqrt{2\pi}\ ; \tag{3a}$$

$$\psi_{\partial G}(x) = -\partial_x\varphi_G(x) = x\varphi_G(x); \tag{3b}$$

$$\psi_{Mh}(x) = \partial_x^2\varphi_G(x) = (x^2-1)\varphi_G(x). \tag{3c}$$

The latter is known as the "Mexican hat" wavelet.

2.1.2. Discrete wavelet transform

We will work in the frame of dyadic ($\lambda = 2$) or triadic ($\lambda = 3$) multi-resolution analysis or "MRA", *à la* Mallat[2], where

$$n_\lambda(L) = \mathrm{int}(\log_\lambda L), \tag{4}$$

is a key quantity: the number of octaves ($\lambda = 2$) or powers of 3 in the data. Here we narrow our focus onto the following subset of (a,b)'s:

$$\begin{cases} a_j(\lambda) = \lambda^j, & j = 0,\ldots,j_{\max} \\ b_{ji}(\lambda) = i\lambda^j, & i = 0,\ldots,\lambda^{j_{\max}-j}-1 \end{cases} \tag{5}$$

where $j_{\max} = n_\lambda(L)-1$. The total number of points in this subset is

$$\mathrm{card}[\{a_j,b_{ji}\}] = \frac{\lambda^{n_\lambda(l)}-1}{\lambda-1}\ . \tag{6}$$

The break-down of this MRA is:

Wavelet coefficients in MRA:	$(\lambda-1)\times\mathrm{card}[\{a_j,b_{ji}\}]$;
Scaling-function coefficient required at $j_{\max}$:	1;
Total number of coefficients in MRA:	$\lambda^{n_\lambda(l)}$.

In the following, we use $I_s(x)$ to designate the indicator function of sub-set S: $I_S(x) = 1$, if $x \in$ S; $I_S(x) = 0$, otherwise.

<u>$\lambda = 2$:</u> The famous Haar basis is spawned by

$$\begin{cases} \varphi_H(x) = I_{[0,2)}(x)/2 \\ \psi_H(x) = -I_{[0,1)}(x)+I_{[1,2)}(x) \end{cases} \tag{7}$$

with the normalization required in (2a). Notice how, apart from a unitary translation, the Haar scaling-function and wavelet in Eq. (7) are piece-wise constant approximations of the Gaussian in Eq. (3a) and its anti-derivative in Eq. (3b).

The computational MRA "trick," leading to algorithms with $O(N)$ complexity[2], is based on the remark that $\psi_H(x)$ in Eq. (7) can be rewritten as $2[-\varphi_H(x/2)+\varphi_H(x/2-1)]$.

$\underline{\lambda = 3}$:

$$\begin{cases} \varphi_3(x) = I_{[0,3)}(x)/3 \\ \psi_a(x) = -I_{[0,1)}(x) \qquad\qquad +I_{[2,3)}(x) \\ \psi_s(x) = +I_{[0,1)}(x) - 2\times I_{[1,2)}(x) + I_{[2,3)}(x) \end{cases} \tag{8}$$

In this natural extension of the generators of the Haar basis in (7), the symmetric wavelet $\psi_s(x)$ —sometimes called the "(French) top-hat" wavelet— is a piece-wise constant approximation to $\psi_{Mh}(x)$, as in (3c) but shifted. This twice-oscillating wavelet resonates with bumps in the field whereas the anti-symmetric wavelet $\psi_s(x)$, the Haar wavelet $\psi_H(x)$ and $\psi_{\partial G}(x)$ all respond to ramps or steps.

2.2. Multifractal analysis

2.2.1. Structure functions:

Structure functions[3] are 2-point statistics for a given "lag" r defined any "order" q:

$$\langle |f(x+r)-f(x)|^q \rangle_{x,f} \sim r^{\zeta(q)} \tag{9}$$

where the subscript "x,f" denotes the spatial (or x-) averaging and an optional ensemble (or f-) averaging. In Eq. (9) we have spelled out the power-law representation of structure functions that we expect in scale-invariant (or "fractal") signals. In practical applications ("physical" fractals), the power-law behavior in (9) applies over a finite scaling range $[r_{min},r_{max}]$.

With wavelets, the structure functions in (9) generalize to:

$$\langle |T_\psi[f](a,b)|^q \rangle_{b,f} \sim a^{\zeta(q)} \tag{10}$$

for $[a_{min},a_{max}]$. In fact, (9) is a special case of (10) for the following choice of wavelet:

$$\psi_{pm}(x) = \delta(x-1) - \delta(x), \tag{11}$$

with $a = r$; Muzy *et al.*[4] call this the "poor man's" wavelet. These authors proceed to describe conditions on f's singularity spectrum and/or ψ's number of oscillations under which the same $\zeta(q)$'s are obtained using (9) and (10), generally with a different set of prefactors however. For $q \geq 0$, all (admissible) wavelets with one or more oscillations are sensitive to all orders of (Hölder) singularity less than unity and greater than zero, i.e., everywhere $f(x)$ is non-differentiable; furthermore, the choice of ψ only affects the prefactor in (10), not the exponent[4,6].

Having established an identity between $\zeta(q)$ exponents using different wavelets, including the degenerate case in (11), it is important to be able to compare the scaling regimes. However, different wavelets have different connections between the scale-parameter a and the lag r. For instance, we should use

$$r_j(\lambda) = (\lambda-1)a_j(\lambda), j = 0,\ldots j_{max} \tag{12a}$$

For $\psi_H(x)$ and $\psi_a(x)$, respectively, in DWTs with $\lambda = 2,3$. There is no general rule for CWTs. One can use the distance between the extrema which yields 2 for $a = 1$ when using $\psi_{\partial G}(x)$; alternatively, one can use

$$r_1 = 2 \times \int_0^\infty x\, \psi(x)\mathrm{d}x \Big/ \int_0^\infty \psi(x)\mathrm{d}x \tag{12b}$$

for any centered anti-symmetric ($\psi(0) = 0$) wavelet; for $\psi_{\partial G}(x)$, this again yields $r_1 = 2$ for $a = 1$.

2.2.2. Partition functions:

In lieu of the wavelet-based generalization of structure functions in (10), one can use the "partition function,"

$$Z(q,a) = \Big\langle \sum_{b\in S_a} |T_\psi[f](a,b)|^q \Big\rangle_{b,f} \tag{13}$$

where S_a is a subset of all positions (b's) that are used to sample the wavelet coefficient for a given scale a. For partition functions, the scaling in Eqs. (9–10) becomes

$$Z(q,a) \sim a^{\tau(q)}. \tag{14}$$

The statistical quantities in (10) and (13–14) are of course related. Operationally (i.e., in terms of estimators), we have

$$\langle |T_\psi[f](a,b)|^q \rangle_{b,f} = Z(q,a) \,/\, \mathrm{card}[S_a] \tag{15}$$

where, in one of the approaches to be described below, card[S_a] is a narrowly-distributed random variable, only weakly dependent of f (hence the above factoring); otherwise, card[S_a] depends only on a and the choice of wavelet ψ. At any rate, the relation between $\tau(q)$ in (14) and $\zeta(q)$ in (10) depends on the spatial (b-wise) sampling strategy.

Continuous spatial sampling: Consider first a CWT approach based on

$$S_a = \{b \in [0,L);\ 0 \le b < L\} \tag{16}$$

where b is discretely sampled on the x-axis and recalling that we assume periodic continuation; so we have card[S_a] $\propto L$ ($= L$, if the x and b share the same grid) in Eq. (15), independently of a, hence $\tau(q) = \zeta(q)$ by examination of (10) and (14–15).

For wavelet choices that happen to belong to DWT bases (e.g., ψ_H or ψ_{Mh}), this CWT approach is amenable to a significant computational enhancement by using a "non-decimated" DWT (ND-DWT) where a is discretely sampled but not b[5]. There is a small cost in the b-sampling to pay:

$$\mathrm{card}[S_a] = L-(\lambda-1)\sum_{j'=0}^{j(a)} \lambda^{j'} = L+1-\lambda^{j(a)+1}$$

where λ is a dividing ratio of the DWT and $j(a)$ is the inverse function of a_j in Eq. (5).

WTMM spatial sampling: Following Muzy *et al.*[4], consider the (continuous) Wavelet Transform Maximum Modulus or "WTMM" approach based on the remark that the wavelet coefficient field $T_\psi[f](a,b)$ defined in Eq. (2) is smooth in both variables. So one can define

$$S_a = \{b \in [0,L);\ |T_\psi[f](a,b)| \text{ is locally max}\}. \tag{17}$$

Here, card[S_a] $\approx L/a$ because, at least for scale-invariant (self-similar) data, extrema in $T_\psi[f](a,b)$ with respect to b necessarily alternate at scales $\approx a$, which is the characteristic smoothing scale of the kernel in Eq. (2a). So we find $\tau(q) = \zeta(q)-1$.

WTMM methodology is far more than a just sampling strategy and the interested reader is referred to recent review papers[6-7]. Indeed, WTMM approaches clarify the deep connections that exist between wavelet theory and multifractal formalism, including powerful analogies with thermodynamics[7].

DWT spatial sampling: Consider now a DWT-based approach with

$$S_a = S_j = \{b \in [0,L);\ b = b_{ji}(\lambda) \text{ from Eq. (5)}\}. \tag{18}$$

Since card[S_a] $= \lambda^{j_{\max}-j} \approx L/a$, as for WTMM sampling, we again find $\tau(q) = \zeta(q)-1$.

By using the "box-car" function $I_{[0,1)} = 2\times\varphi_H(x/2)$ instead of the wavelet in (2a), we retrieve the (dyadic) "box-counting" method. In turn, this leads to the original[8] definition of $\tau(q)$ for a (non-negative) measure $\mu(x)$:

$$\sum_{b\in S_a}\Big[\int_b^{b+a}\mu(x)\mathrm{d}x\Big]^q = \sum_{b\in S_a}|aT_{\varphi_H}[\mu](a,b)|^q \sim a^{\tau(q)}. \tag{19}$$

Muzy *et al.*[4] show that, if the measure $\mu(x)$ is singular (vanishes everywhere except on a set of Lebesgue measure 0, e.g., Cantor's measure or its multifactal counterparts), then using the scaling function φ or a wavelet ψ does not influence the outcome $\tau(q)$ in (19).

2.3. Illustration with cloud data

Figure 1 shows two traces of cloud liquid water content (mass of all droplets per unit of volume) measured during aircraft penetrations into a marine stratocumulus deck; see reference 9. for details. The variability and its change in space —the variability of the variability— are remarkable but not untypical in geophysics.

Figure 2 shows the similar scaling at $q = 2$ obtained elsewhere[10] for structure functions and selected wavelet counterparts using various sampling procedures on the data in panel (a). For obvious reasons, the DWT sampling strategies (represented by ×'s and +'s in Fig. 2) yield noisier estimates but they has the advantage of MRA's computational efficiency. This makes it an attractive approach for "on-line" multifractal analysis of data, as fast as it is collected. A systematic comparison of wavelet-multifractal data analyses is in preparation.

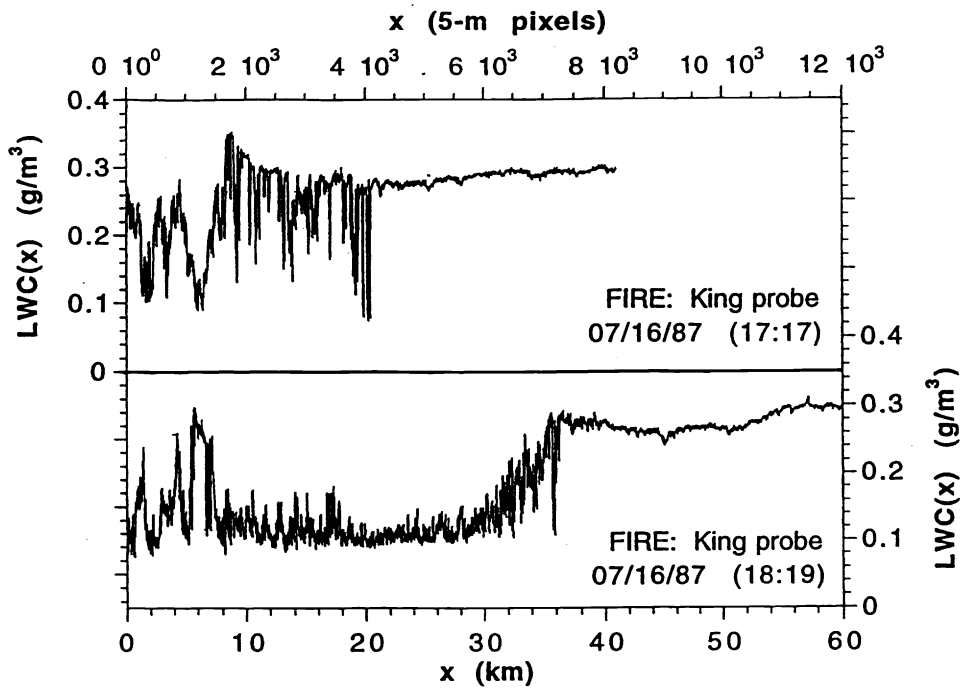

Figure 1: *Two runs of liquid water density in marine boundary-layer clouds.* These data were obtained off the coast of Southern California

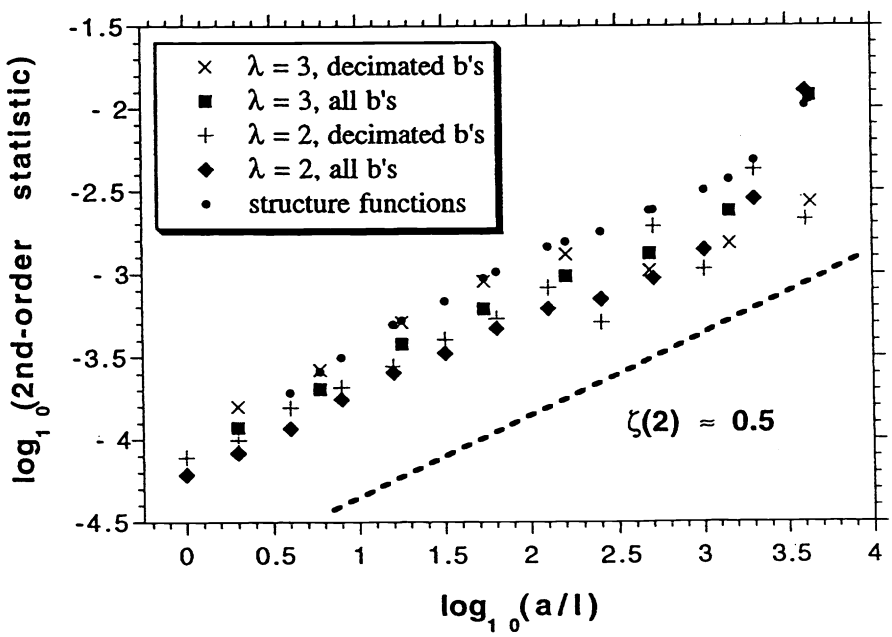

Figure 2: *Structure functions and wavelet-based counterparts for data in Fig. 1.* Within the accuracy of the sampling, the various approaches all yield an estimate of the scaling exponent $\zeta(2) \approx 0.5$. This corresponds (Wiener-Khinchin theorem for power-law statistics[3]) to an exponent $\beta = \zeta(2)+1 \approx 1.5$ for the energy spectrum $E_f(k) \propto \|F[f](k)\|^2 \propto 1/k^\beta$ where $F[f]$ is the Fourier transform of f.

3. WAVELET-MULTIFRACTAL ANALYSIS AND MODELING IN TWO DIMENSIONS

3.1. Definitions in 2D (isotropic case)

We now assume the data is given on a regular 2D grid:

$$f(\boldsymbol{x}) = f(x_1,x_2),\ 0 \le x_1 < L_1,\ 0 \le x_2 < L_2 \tag{20}$$

with, for simplicity, unitary constants ℓ_1 and ℓ_2 (ℓ_1 and ℓ_2 can of course differ for instrumental reasons). Two-dimensional generalizations of the Gaussian wavelets in (3a–c) lead either to scalar or vector formulations. In the following, we will use

$$\varphi_G(\boldsymbol{x}) = \frac{1}{2\pi}\exp\left[\frac{-\boldsymbol{x}^2}{2}\right] = \frac{1}{2\pi}\exp\left[\frac{-(x_1{}^2+x_2{}^2)}{2}\right]. \tag{21}$$

3.1.1. CWTs with scalar wavelets:

As an example, the CWT based on the popular 2D Mexican-hat is:

$$T_{\psi_{Mh}}[f](a,\boldsymbol{b}) = \frac{1}{a^2}\int f(\boldsymbol{x})\psi_{Mh}\left(\frac{\boldsymbol{x}-\boldsymbol{b}}{a}\right) d^2\boldsymbol{x} \tag{22a}$$

where

$$\psi_{Mh}(\boldsymbol{x}) = \nabla^2\varphi_G(\boldsymbol{x}) = (x_1{}^2+x_2{}^2 - 2)\varphi_G(x_1,x_2). \tag{22b}$$

3.1.2. CWTs with vector wavelets:

The Gaussian's 1st-order partial derivatives can also be used in the pair of transforms:

$$T_{\psi_m}[f](a,\boldsymbol{b}) = \frac{1}{a^2}\int f(\boldsymbol{x})\psi_m\left(\frac{\boldsymbol{x}-\boldsymbol{b}}{a}\right) d^2\boldsymbol{x}\ (m = 1,2) \tag{23a}$$

where

$$\psi(\boldsymbol{x}) = \{\psi_1(\boldsymbol{x}),\psi_2(\boldsymbol{x})\}^T = -\left\{\frac{\partial}{\partial x_1}, \frac{\partial}{\partial x_2}\right\}^T \varphi_G(\boldsymbol{x}), \tag{23b}$$

superscript "T" meaning transpose. These filters are commonly used in edge-detection applications.

Whether the CWT's outcome is scalar or vector, the wavelet domain is:

$$\begin{cases} 0 < a \le L = \min_m\{L_m,\ m = 1,2\} \\ 0 \le b_m < L\ (m = 1,2) \end{cases}, \tag{24}$$

assuming periodic extensions.

3.1.3. DWTs with λ = 2,3:

In isotropically discretized wavelet space, the scale parameter a_j is as in Eq. (5), but position naturally become a vector:

$$\boldsymbol{b}_{j,i}(\lambda) = \boldsymbol{i}\lambda^j,\ i_m = 0,\ldots,\lambda^{j_{max}-j}-1\ (m = 1,2), \tag{25}$$

and the total number of points is

$$\mathrm{card}[\{a_j,\boldsymbol{b}_{j,i}\}] = \frac{\lambda^{2n_\lambda(L)}-1}{\lambda^2-1}. \tag{26}$$

The break-down of a 2D MRA using tensor products of the basis-generators in (7–8) is:

2D MRA wavelet coefficients:	$(\lambda^2-1)\times\mathrm{card}[\{a_j,\boldsymbol{b}_{ji}\}]$;
scaling-function coefficient required at j_{max}:	1;
total number of coefficients in 2D MRA:	$(\lambda^2)^{n_\lambda(L)}$.

Because the scaling functions and wavelets in one-dimensional MRA can be mapped to the 0th-, 1st- and 2nd-order derivatives of the Gaussian, their λ^2 different tensor products are akin to the various partial- and crossed derivatives of the 2D Gaussian. For instance, $\varphi_H(x_1)\psi_H(x_2)$ or $\varphi_3(x_1)\psi_a(x_2)$ will approximate $\psi_2(\boldsymbol{x})$.

3.2. Isotropic partition functions

There is no fundamental difference between 1D and 2D multifractal analyses, standard or wavelet-based, as long as it is kept isotropic (no preferred directions at any scale). Partition functions still scale as $Z(q,a) \sim a^{\tau(q)}$; only the detailed way they are computed changes.

Scalar-wavelet approach using Eqs. (22a,b):

$$Z(q,a) = \Big\langle \sum_{\boldsymbol{b}\in S_a} |T_\psi[f](a,\boldsymbol{b})|^q \Big\rangle_f \tag{27}$$

Vector-wavelet approach using Eqs. (23a,b):

$$Z(q,a) = \Big\langle \sum_{\boldsymbol{b}\in S_a} \|\boldsymbol{T}_\psi[f](a,\boldsymbol{b})\|^q \Big\rangle_f \tag{28a}$$

where

$$\|\boldsymbol{T}_\psi[f](a,\boldsymbol{b})\| = \sqrt{T_{\psi_1}[f](a,\boldsymbol{b})^2 + T_{\psi_2}[f](a,\boldsymbol{b})^2}\,. \tag{28b}$$

Two-dimensional structure functions can be defined[3], with and without isotropy, as $\langle |f(\boldsymbol{x}+\boldsymbol{r})-f(\boldsymbol{x})|^q\rangle_{\boldsymbol{x},f}$ but they have rarely been used in data analysis, except for[16] $q = 2$. The closest wavelet analog is $\langle \|\boldsymbol{T}_\psi[f](a,\boldsymbol{b})\|^q\rangle_{\boldsymbol{b},f} = Z(q,a)/\mathrm{card}[S_a]$ from (28a) and it scales as $a^{\zeta(q)}$.

As in 1D, there are several sampling strategies: continuous, WTMM, and DWT.

Continuous spatial sampling:

$$S_a = \{\boldsymbol{b};\ 0 \le b_1, b_2 < l\} \tag{29}$$

We again must account for the dimensionality effect on the scaling: $\tau_c(q) = \zeta(q) = \tau(q)+2$, since $\mathrm{card}[S_a] = L^2$ for all a's. Because 2D datasets tend to be quite large, this is a situation where the computational acceleration of ND-DWTs is welcome.

WTMM spatial sampling:

$$S_a = \{\boldsymbol{b};\ \|\boldsymbol{T}_\psi[f](a,\boldsymbol{b})\| \text{ is locally max}\} \tag{30}$$

with $\mathrm{card}[S_a] \approx (L/a)^2$ because of correlations extending over a range $\approx a$ in wavelet space. Arrault *et al.*[17] successfully applied 2D-WTMM methodology to synthetic surfaces, both Gaussian and multifractal, with specified roughness, as well as to some high-resolution satellite images of turbulent cloud structures.

DWT spatial sampling:

$$S_a = S_j = \{\boldsymbol{b};\ \boldsymbol{b} = \boldsymbol{b}_{j,i}(\lambda)\} \tag{31}$$

with $\mathrm{card}[S_a] = \lambda^{2(j_{\max}-j)} \approx (L/a)^2$. Here again the disadvantage of increased statistical noise is off-set by the possibility of $O(N)$ computational efficiency in applications where it is desirable to obtain multifractal statistics almost as fast as the images are captured.

3.3. Approaches to anisotropy

We list here a few ways of describing anisotropy in 2D data.

3.3.1. Using scalar wavelets:

Here the scale parameter becomes a vector

$$\boldsymbol{a} = (a_1, a_2)^{\mathrm{T}} \tag{32}$$

in the generalized form of Eq. (22a):

$$T_\psi[f](\boldsymbol{a},\boldsymbol{b}) = \frac{1}{a_1 a_2}\int f(\boldsymbol{x})\psi\Big(\frac{x_1-b_1}{a_1}, \frac{x_2-b_2}{a_2}\Big)\, \mathrm{d}^2\boldsymbol{x}. \tag{33}$$

The wavelet itself can be axi-symmetric, as in $\psi_{\mathrm{Mh}}(\boldsymbol{x})$; or else it can have less symmetry, as in $(\partial/\partial x_1)(\partial/\partial x_2)\varphi_G(\boldsymbol{x})$ which is a filter for "checker-board" patterns illustrated in Fig. 3, or $\psi_1(\boldsymbol{x}) = -(\partial/\partial x_1)\varphi_G(\boldsymbol{x})$ which is a standard edge detector.

3.3.2. Using vector wavelets:

Here we can simply use the directional information in the wavelet transform pair (23a):

$$\begin{cases} \cos\alpha(a,\boldsymbol{b}) = T_{\psi_1}[f](a,\boldsymbol{b}) / \|\boldsymbol{T}_\psi[f](a,\boldsymbol{b})\| \\ \sin\alpha(a,\boldsymbol{b}) = T_{\psi_2}[f](a,\boldsymbol{b}) / \|\boldsymbol{T}_\psi[f](a,\boldsymbol{b})\| \end{cases}. \tag{34}$$

A quantitative test of anisotropy is to examine the possibly scale-dependent distribution of α for the existence of modes.

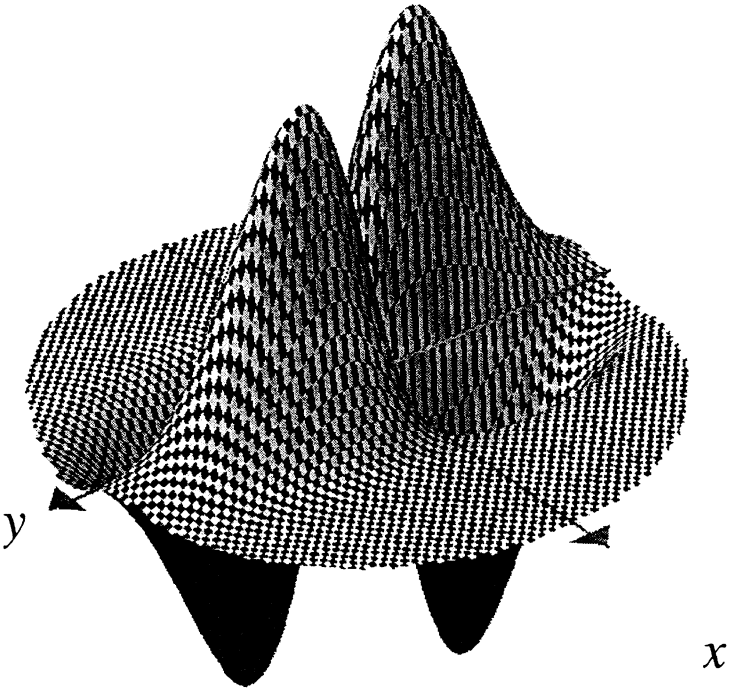

Figure 3: *Anisotropic 2D wavelet with $a_2/a_1 = 2$ based on the crossed partial derivatives of the Gaussian.*

3.3.3. Using custom multi-resolution analysis:

A simple and potentially useful way of measuring and simulating anisotropy is to use (I)DWTs based on tensor products of different wavelet bases on each axis. For instance, the dyadic and triadic scaling functions and wavelets defined in Eqs. (7–8).

Given some 2D data (possibly on an oblong support), we first decide which axis is assigned to the dyadic branching and which to the triadic, e.g., $\lambda_x = \lambda_1 = 3$ (horizontal), $\lambda_z = \lambda_2 = 2$ (vertical). We then compute

$$n_m(\lambda_m) = \mathrm{int}[\log_{\lambda_m} L_m] \ (m = 1,2) \tag{35}$$

and reckon the number of cascade steps:

$$n_c(L) = n_c(L_1,L_2) = \min\{n_1(\lambda_1),n_2(\lambda_2)\}. \tag{36}$$

The constants used in the anisotropic (I)DWT —using a two-dimensional MRA— are given in Fig. 4a. Figure 4b is a schematic of this MRA where the total number of points is

$$\mathrm{card}[\{\boldsymbol{a}_j,\boldsymbol{b}_{j,i}\}] = \frac{(\lambda_1\lambda_2)^{n_c(l)}-1}{\lambda_1\lambda_2-1}. \tag{37}$$

The break-down of the custom two-dimensional MRA is:

2D MRA wavelet coefficients:	$(\lambda_1\lambda_2-1)\times\mathrm{card}[\{\boldsymbol{a}_j,\boldsymbol{b}_{ji}\}]$;
Scaling-function coefficient required at $j_{\max}$:	1;
Total number of coefficients in 2D MRA:	$(\lambda_1\lambda_2)^{n_c(L)}$.

Following the procedure outlined in the Appendix, we can use the IDWT in Figs. 4a–b to generate anisotropic cascade models with radically different properties when sampled or integrated in the horizontal (#1) and vertical (#2) directions.

$\varphi(x,y) = 1/6$ $\psi_1(x,y) = +1/3$ $\psi_2(x,y) = -1/2$ $\psi_3(x,y) = -1$ $\psi_4(x,y) = +1/2$ $\psi_5(x,y) = +1$	$\varphi(x,y) = 1/6$ $\psi_1(x,y) = +1/3$ $\psi_2(x,y) = 0$ $\psi_3(x,y) = 0$ $\psi_4(x,y) = -1$ $\psi_5(x,y) = -2$	$\varphi(x,y) = 1/6$ $\psi_1(x,y) = +1/3$ $\psi_2(x,y) = +1/2$ $\psi_3(x,y) = +1$ $\psi_4(x,y) = +1/2$ $\psi_5(x,y) = +1$
$\varphi(x,y) = 1/6$ $\psi_1(x,y) = -1/3$ $\psi_2(x,y) = -1/2$ $\psi_3(x,y) = +1$ $\psi_4(x,y) = +1/2$ $\psi_5(x,y) = -1$	$\varphi(x,y) = 1/6$ $\psi_1(x,y) = -1/3$ $\psi_2(x,y) = 0$ $\psi_3(x,y) = 0$ $\psi_4(x,y) = -1$ $\psi_5(x,y) = +2$	$\varphi(x,y) = 1/6$ $\psi_1(x,y) = -1/3$ $\psi_2(x,y) = +1/2$ $\psi_3(x,y) = -1$ $\psi_4(x,y) = +1/2$ $\psi_5(x,y) = -1$

$f(x,y+\ell) = \langle f,\varphi\rangle$ $- \langle f,\psi_1\rangle$ $+ (\langle f,\psi_2\rangle$ $-\langle f,\psi_3\rangle/2)/2$ $+ (\langle f,\psi_4\rangle$ $-\langle f,\psi_5\rangle/2)/6$	$f(x+\ell,y+\ell) = \langle f,\varphi\rangle$ $- \langle f,\psi_1\rangle$ $+ 0$ $+ 0$ $- (\langle f,\psi_4\rangle$ $-\langle f,\psi_5\rangle/2)/3$	$f(x+2\ell,y+\ell) = \langle f,\varphi\rangle$ $- \langle f,\psi_1\rangle$ $- (\langle f,\psi_2\rangle$ $-\langle f,\psi_3\rangle/2)/2$ $+ (\langle f,\psi_4\rangle$ $-\langle f,\psi_5\rangle/2)/6$
$f(x,y) = \langle f,\varphi\rangle$ $+ \langle f,\psi_1\rangle$ $+ (\langle f,\psi_2\rangle$ $+\langle f,\psi_3\rangle/2)/2$ $+ (\langle f,\psi_4\rangle$ $+\langle f,\psi_5\rangle/2)/6$	$f(x+\ell,y) = \langle f,\varphi\rangle$ $+ \langle f,\psi_1\rangle$ $+ 0$ $+ 0$ $- (\langle f,\psi_4\rangle$ $+\langle f,\psi_5\rangle/2)/3$	$f(x+2\ell,y) = \langle f,\varphi\rangle$ $+ \langle f,\psi_1\rangle$ $- (\langle f,\psi_2\rangle$ $+\langle f,\psi_3\rangle/2)/2$ $+ (\langle f,\psi_4\rangle$ $+\langle f,\psi_5\rangle/2)/6$

Figure 4a: *Anisotropic 2D multi-rresolution analysis.* Linear algebra for DWT and IDWT.

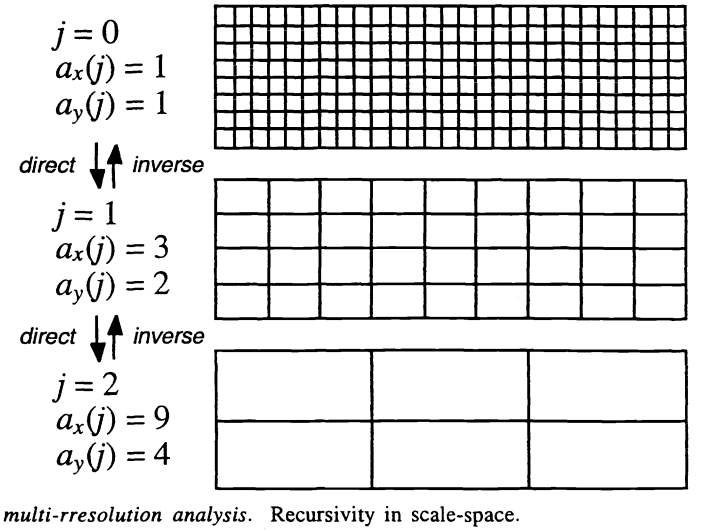

Figure 4b: *Anisotropic 2D multi-rresolution analysis.* Recursivity in scale-space.

For instance, we can dial a "bounded" cascade behavior in the horizontal, hence a degree of stochastic continuity and an associated degree of nonstationarity (2-point correlations are long-range). At the same time, we can prescribe "singular" cascade behavior in the vertical, hence almost everywhere discontinuity and the associated stationarity (2-point correlations are short-range). We thus obtain $\tau_x(q) \neq \tau_z(q)$ in Eqs. (13–14). Assuming WTMM or DWT sampling is invoked, we have $\tau_x(q) = \zeta(q)-1$ from Eq. (A6) using any admissible wavelet in the partition function $Z(q,a)$, and $\tau_z(q) = \tau(q)$ from Eq. (A5) using either a scaling function or a wavelet in $Z(q,a)$.

To achieve this, we take:

$$T_{\varphi_3\psi_H}[\ln f](\boldsymbol{a}_j,\boldsymbol{b}_{ji}) = T_{\psi_H}[\cdot](a_{yj},\cdot) \qquad \text{from Eq. (A4a);} \tag{38a}$$

$$T_{\psi_a\varphi_H}[\ln f](\boldsymbol{a}_j,\boldsymbol{b}_{ji}) = T_{\psi_a}[\cdot](a_{xj},\cdot) \qquad \text{from Eq. (A9a);} \tag{38b}$$

$$T_{\psi_a\psi_H}[\ln f](\boldsymbol{a}_j,\boldsymbol{b}_{ji}) = 0; \tag{38c}$$

$$T_{\psi_s\varphi_H}[\ln f](\boldsymbol{a}_j,\boldsymbol{b}_{ji}) = T_{\psi_s}[\cdot](a_{xj},\cdot) \qquad \text{from Eq. (A9b);} \tag{38d}$$

$$T_{\psi_s\psi_H}[\ln f](\boldsymbol{a}_j,\boldsymbol{b}_{ji}) = 0; \text{ and} \tag{38e}$$

$$T_{\varphi_3\varphi_H}[\ln f](\boldsymbol{a}_{j_{\max}},\boldsymbol{0}) = \sum_j \left(T_{\varphi_H}[\cdot](a_{xj},\cdot)+T_{\varphi_3}[\cdot](a_{yj},\cdot)\right) \qquad \text{from Eqs. (A4b) and (A9c) respectively.} \tag{38f}$$

Figure 5 shows two specific 729×64 (n_c = 6) realizations of this model for $p_1 = 0.3$, $p_2 = 0.55$ and $H = 1/3$ in the horizontal direction, $p = 0.2$ and $H = 0$ in the vertical, with square pixels at the smallest scale ($\ell_1 = \ell_2 = 1$).

The above choice of parameters, hence of marginal (x- or z-projected) properties, is not arbitrary. The Earth's cloudy atmosphere is strongly stratified and clouds tend to appear in well-defined layers —hence the singular model for the vertical unfolding. Inside these layers, long-range correlations are observed in the horizontal direction[9-10]. —hence the bounded cascade. Actually this was the very first application of the bounded model[18]. Recently developed radars operating in at mm wavelengths are able to probe vertical and horizontal cloud structure. Specifically, we intend to apply the above MRA in analysis mode to the liquid water density field in boundary-layer clouds, as the prevailing wind advects them by a vertically pointing mm-radar system at sites in Oklahoma, Alaska, and the tropical Pacific extensively instrumented by DOE's ARM (Atmospheric Radiation Measurement) program.

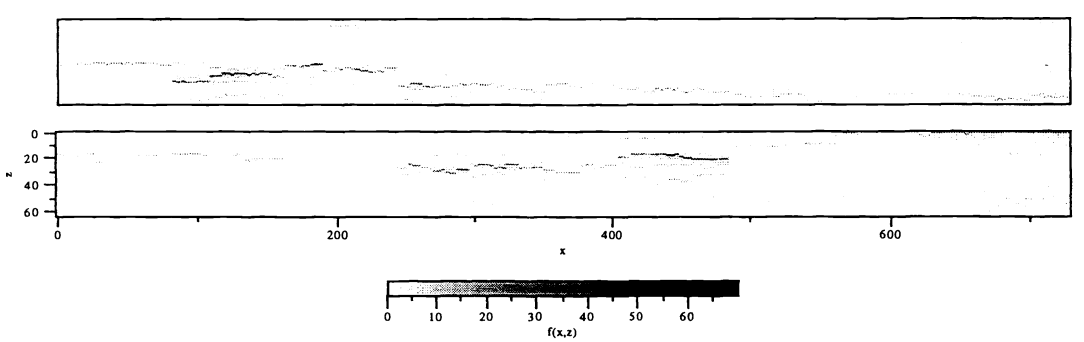

Figure 5: *Two realizations of a highly variable and strongly anisotropic cascade processes generated by IDWT, with unit mean.*

4. SUMMARY

We surveyed, from an algorithmic stand-point, various ways of performing multifractal data analyses using wavelet transforms. The methods range from the sophisticated (but labor intensive) WTMM approach to the simple (yet overlooked) utilization of DWTs. The inevitable loss in estimation accuracy is offset by a significant gain in efficiency: thanks to MRA algorithms only $O(N)$ operations are required. An $O(N\log N)$ compromise is to use "non-decimated" DWTs where the scale parameter is still incremented logarithmically but the wavelet's position is sampled continuously.

Going from 1D to 2D, we show how a tensor product of dyadic and triadic DWTs can be used to simulate (here) and measure (elsewhere) strong deviations from statistical isotropy, as are observed in many natural systems. The highly stratified structure of the Earth's cloudy atmosphere is our primary target. The wavelet coefficients from the new MRA will characterize at once the anisotropy and the long-range correlations in a multifractal analysis scheme.

APPENDIX: CASCADE MODELING WITH THE INVERSE DWT (IDWT) IN ONE DIMENSION

In this appendix, we briefly describe methods to generate mono- and multifractal data with known properties in discrete wavelet space[11]. The length of each realization is set by

$$L = \lambda^{j_{\max}+1} \tag{A1}$$

where $\lambda = 2$ or 3. To obtain long signals, $n_\lambda(L) = j_{\max}+1$ will generally be taken $\gg 1$.

A.1. Dyadic cascades ($\lambda = 2$)

A.1.1. Fractional Brownian motion (fBm):

It has been shown[12] that a close analog of fBm is obtained by randomly activating DWT coefficients. Specifically, for the Haar basis (7) with the normalization convention in (2a), this algorithm reads as

$$T_{\psi_H}[fBm](a_j,b_{ji}) = N(0,1)(2a_j)^{H_2} \tag{A2a}$$

where H_2 is the sole parameter and is normally set between 0 and 1. The $N(0,1)$'s are independent pseudo-Gaussian deviates with zero-mean and unit-variance. The L–1 wavelet coefficients in (A2a) are completed by

$$T_{\varphi_H}[fBm](a_{j_{\max}},0) = 0 \tag{A2b}$$

in the MRA decomposition. The signal $f(x)$ is synthesized by IDWT.

The recipe in Eq. (A2a) leads directly to

$$\zeta(q) = qH_2 \tag{A3}$$

in Eq. (10). This linear (or "monoscaling") function is the hallmark of a *mono*fractal model. There is a Wiener-Khinchin type relation for nonstationary processes with stationary increments (such as fBm) that, in the case of power-laws, connects $\zeta(2)$ to the spectral exponent in $E_f(k) \propto \|F[f](k)\|^2 \propto 1/k^\beta$ where $F[f]$ is the Fourier transform of f; specifically, we have[3]:

$$\beta = \zeta(2)+1.$$

For the type of fBm defined by Eq. (A2a,b), this yields[12] $\beta = 2H_2+1$ which normally varies between 1 (the "$1/f$" noise limit) and 3 (the everywhere continuous, almost everywhere differentiable limit). If $H_2 < 0$, we obtain stationary scaling noises with $\beta = 1-2|H_2| < 1$ and $\zeta(q) \equiv 0$; for $H_2 > 1$, the result is a smooth function with $\beta > 3$ and $\zeta(q) \equiv q$. The cross-over from stationary to nonstationary scaling behavior at $\beta = 1$ (exactly $1/f$ noise) is discussed in detail in references 9. and 20.

A.1.2. Multiplicative cascades, singular (p-models) and bounded (p,H-models):

As a counterpoint to fBm's characteristic monoscaling ($\zeta(q)/q = constant$) and purely additive construction, we propose bounded multiplicative cascade models[13,17]. Their construction can be recast deterministically in a DWT context using the Haar basis:

$$T_{\psi_H}[\ln f](a_j,b_{ji}) = \pm\ln\left(\frac{1+(2p-1)(2a_j/L)^H}{1-(2p-1)(2a_j/L)^H}\right) \tag{A4a}$$

where the sign is random, and

$$T_{\varphi_H}[\ln f](a_{j_{\max}},0) = \frac{1}{2}\sum_{j=0}^{j_{\max}} \ln(1-(2p-1)^2(2a_j/L)^{2H}). \tag{A4b}$$

The "boundedness" parameter H is non-negative (with 0 being the "singular" limit), while p varies between 0 and 1/2 (the homogeneous limit). Notice that the wavelet coefficients in (4a) are not strictly power law with respect to scale a, except in the singular limit $H = 0$ (where they are degenerate, i.e., scale-independent). In other words, to highlight the scaling we need to take the small-scale ($a/L \ll 1$) limit where a 1st-order Taylor expansion of Eq. (A4a) leads to

$$T_{\psi_H}[\ln f](a_j,b_{ji}) \approx \pm 2(2p-1)(2a_j/L)^H,$$

hence $\langle |T_{\psi_H}[\ln f](a,\cdot)|^q\rangle \sim a^{qH}$ and, at 2nd-order, we have $\beta = 2H+1$. So the structure function scaling exponents for $\ln f(x)$ are given by $\zeta(q) = q\times\min\{H,1\}$ which are identical to those of fBm in Eq. (A3) as long as $0 < H < 1$.

To obtain $f(x)$ itself, we just exponentiate the outcome of the IDWT. In the logarithms, we can then recognize respectively the ratio and product of the two non-vanishing multiplicative "weights" respectively in (A4a) and under the summation in (4b). Interestingly, the original algorithm proceeds from largest to smallest scales whereas the IDWT goes inversely. At any step in the recursive sub-division by 2, the two weights are applied to the two sub-intervals; this just amounts to shifting a certain fraction the "mass" from one side to the other in a random direction. In this so-called[14] "micro-canonical" model the weights are purposefully designed to exactly conserve the total measure or "mass", at each cascade step and in each realization.

For $H = 0$, the mass fraction in the transfer remains constant and we retrieve the simple one-parameter "p-model" that Meneveau and Sreenivasan[15] proposed for the dissipation field in turbulence. These authors showed that

$$\tau(q) = -\log_2[p^q+(1-p)^q] \tag{A5}$$

using the box-counting algorithm in Eq. (19) for the singularity analysis, and that $\beta = \tau(2) = -\log_2[1-2p(1-p)] \leq 1$. Figure A1a shows an example with $p = 0.25$ and 12 cascade steps and Fig. A2a shows its logarithm. In summary, this strictly positive stationary *multi*fractal field with unit average value results from exponentiating a *mono*fractal (exactly) $1/f$ noise field,† in this case, with a binomial 1-point probability density function (PDF) centered on the negative value in Eq. (A4b) with $H = 0$.

For $H > 0$, Marshak *et al.*[13] showed that the model has

$$\zeta(q) = \min\{qH,1\} \tag{A6}$$

independently of p, using the qth-order structure functions in Eq. (9), thus confirming the 2nd-order result of Cahalan *et al.*[18] that $\beta = \min\{2H,1\}+1 > 1$. Since $\zeta(q)$ is not linear in q (except in the singular/degenerate limit $H \rightarrow 0$), we are dealing with a multifractal function space. See Fig. A1b for a random sample and Fig. A2b for its log; in this example, we set $H = 1/3$, hence $\beta = \zeta(2)+1 = \min\{2/3,2\}+1 = 5/3$. In summary, these strictly positive unit-mean nonstationary *multi*fractal functions result from exponentiating a *mono*fractal $1/f^\beta$ noises with $\beta > 1$, in this case, with a quasi-Gaussian[18] 1-point PDF centered on the negative value in Eq. (A4b). As far as we know, this mono/multi-fractal connection had not been made before; the extent of its generality beyond bounded cascades remains an open question.

A.2. Triadic cascades ($\lambda = 3$)

A.2.1. Fractional Brownian motion:

Generalization of the above Haar-based model for fBm-type processes to this case is straightforward; we just state the recipe:

$$T_{\psi_a}[fBm](a_j,b_{ji}) = N(0,1)(2a_j)^{H_2}; \tag{A7a}$$

$$T_{\psi_s}[fBm](a_j,b_{ji}) = N(0,1)(6a_j)^{H_2}; \tag{A7b}$$

$$T_{\varphi_3}[fBm](a_{j_{\max}},0) = 0. \tag{A7c}$$

A.2.2. Multiplicative cascades:

Micro-canonical conservation allows for 2 parameters in this case; the 3 non-vanishing weights are:

$$W_1(j,i) = 1+(3p_1-1)(3a_j/L)^H; \tag{A8a}$$

$$W_2(j,i) = 1+(3p_2-1)(3a_j/L)^H; \tag{A8b}$$

$$W_3(j,i) = 3-W_1(j,i)-W_2(j,i). \tag{A8c}$$

Letting $\{k_1,k_2,k_3\} = \text{perm}\{1,2,3\}$ denote a random permutation of the indices, the DWT coefficients are then computed as:

$$T_{\psi_a}[\ln f](a_j,b_{ji}) = \ln[W_{k_3}(j,i)/W_{k_1}(j,i)]; \tag{A9a}$$

$$T_{\psi_s}[\ln f](a_j,b_{ji}) = \ln[W_{k_3}(j,i)W_{k_1}(j,i)/W_{k_2}(j,i)^2]; \tag{A9b}$$

$$T_{\varphi_3}[\ln f](a_{j_{\max}},0) = \frac{1}{3}\sum_j \ln[W_1(j,i)W_2(j,i)W_3(j,i)]. \tag{A9c}$$

† Using Fourier-space methods rather than wavelets, Schertzer and Lovejoy[19] obtain a similar result for log-normal as well as log-Lévy cascade models.

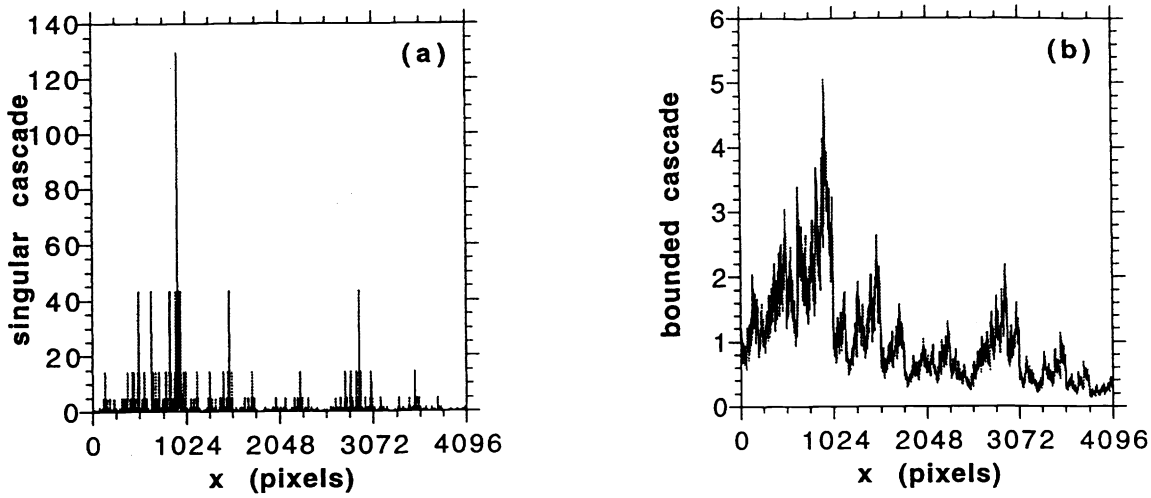

Figure A1: *Multiplicative cascade models.* **(a)** Random multifractal measure, a "p-model" described in the text. **(b)** Random multifractal function, a "p,H-model" described in the text.

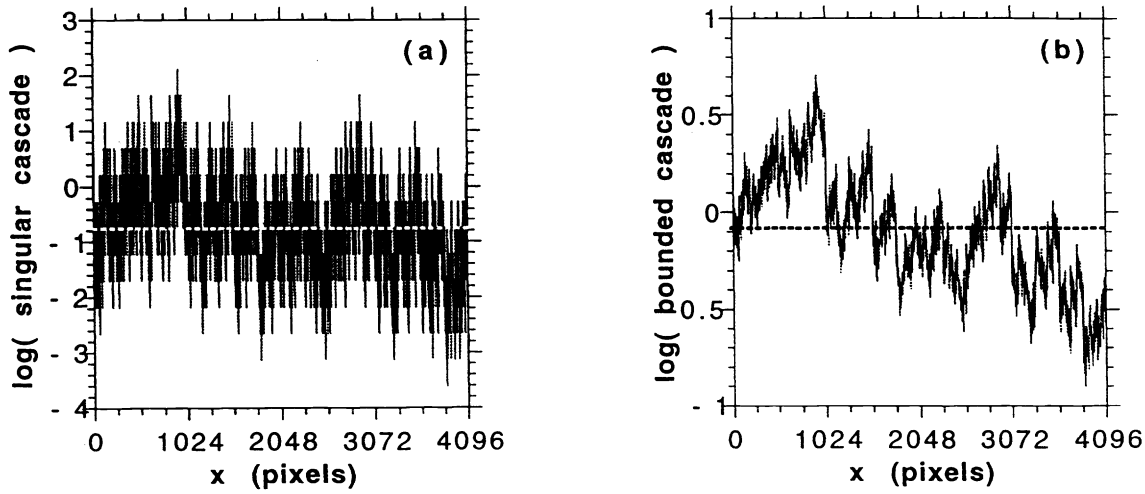

Figure A2: *Additive cascade models.* **(a)** Exactly binomial "$1/f$" noise from the logarithm of the random multifractal measure in Fig. A1a, cf. Eqs. (A4a,b) with $H = 0$ and $p = 0.25$. **(b)** Approximately Gaussian noise with asymptotic scaling in "$1/f^{\beta}$" ($\beta>1$) from the logarithm of the random multifractal function in Fig. A1b, cf. Eqs. (A4a,b) with $H = 1/3$ and $p = 0.25$.

ACKNOWLEDGMENTS

This work was supported financially by the Environmental Sciences Division of U.S. Department of Energy (under grant DE-A105-90ER61069 to NASA's Goddard Space Flight Center) as part of the Atmospheric Radiation Measurement (ARM) program, as well as with a NATO Collaborative Scientific Research Grant. We thank A. Arnéodo, E. Bacry, R. Cahalan, A. Fournier, S. Lovejoy, J.–F. Muzy, R. Pincus, S. Roux, D. Schertzer, and W. Wiscombe for many fruitful discussions.

REFERENCES

1. A. Arnéodo *et al.*, *Ondelettes, Multi-fractales et Turbulences – de l'ADN aux Croissances Cristalines* (Diderot, Paris, 1996); English version in preparation.
2. S. Mallat, "A theory for multiresolution signal decomposition: The wavelet representation," *IEEE Trans. Pattern Anal. Mach. Intel.* **11**, pp. 674–693, 1989.
3. A. S. Monin and A. M. Yaglom, *Statistical Fluid Mechanics*, Vol. 2, MIT Press, Boston, 1975.
4. J.–F. Muzy, E. Bacry, and A. Arnéodo, "Multifractal formalism for fractal signals: The structure-function approach versus the wavelet-transform modulus-maxima method," *Phys. Rev. E* **47**, pp. 875–884, 1993.
5. O. Rioul and M. Vetterli, "Wavelets and signal processing," *IEEE Signal Processing Magazine* **8**, pp. 14–38, 1991.
6. J.–F. Muzy, E. Bacry, and A. Arnéodo, "The multifractal formalism revisited with wavelets," *Int. J. of Bifurcation and Chaos* **4**, pp. 245–302, 1994.
7. A. Arnéodo, E. Bacry, and J.–F. Muzy, "The thermodynamics of fractals revisited with wavelets," *Physica A* **213**, pp. 232–275, 1995.
8. T. C. Halsey, M. H. Jensen, L. P. Kadanoff, I. Procaccia, and B. I. Shraiman, "Fractal measures and their singularities: The characterization of strange sets," *Phys. Rev. A* **33**, pp. 1141–1151, 1986.
9. A. Davis, A. Marshak, W. J. Wiscombe, and R. F. Cahalan, "Scale-invariance in liquid water distributions in marine stratocumulus, Part I, Spectral properties and stationarity issues," *J. Atmos. Sci.* **53**, pp. 1538–1558, 1996.
10. A. Marshak, A. Davis, W. J. Wiscombe, and R. F. Cahalan, "Scale-invariance of liquid water distributions in marine stratocumulus, Part 2 – Multifractal properties and intermittency issues," *J. Atmos. Sci.* **54**, pp. 1423–1444, 1997.
11. R. Benzi, L. Biferale, A. Crisanti, G. Paladin, M. Vergassola, and A. Vulpani, "A random process for the construction of multiaffine fields,".*Physica D* **65**, pp. 352–358, 1993.
12. P. Flandrin, "Wavelet analysis and synthesis of fractional Brownian motion," *IEEE Trans. Inform. Theory* **38**, pp. 910–917, 1992.
13. A. Marshak, A. Davis, R. F. Cahalan, and W. J. Wiscombe, "Bounded cascade models as non-stationary multifractals," *Phys. Rev. E* **49**, pp. 55–69, 1994.
14. B. B. Mandelbrot, "Intermittent turbulence in self-similar cascades: Divergence of high moments and dimension of the carrier," *J. Fluid Mech.* **62**, pp. 331–358, 1974.
15. C. Meneveau, and K.R. Sreenivasan, "Simple multifractal cascade model for fully developed turbulence," *Phys. Rev. Lett.* **59**, pp. 1424–1427, 1987.
16. G. Christakos, *Random Fields in Earth Sciences*, Academic, San Diego, 1992.
17. J. Arrault, A. Arnéodo, A. Davis, and A. Marshak, "Wavelet-based multifractal analysis of rough surfaces – Application to cloud models and satellite data," *Phys. Rev. Lett.* **79**, pp. 75–78, 1997.
18. R. F. Cahalan, W. Ridgway, W. J. Wiscombe, T. L. Bell, and J. B. Snider, "The albedo of fractal stratocumulus clouds," *J. Atmos. Sci.* **51**, pp. 2434–2455, 1994.
19. D. Schertzer, and S. Lovejoy, "Physical modeling and analysis of rain and clouds by anisotropic scaling multiplicative processes," *J. Geophys. Res.*, **92**, pp. 9693–9714, 1987.
20. A. Davis, A. Marshak, and W. Wiscombe, "Wavelet-Based Multifractal Analysis of Nonstationary and/or Intermittent Geophysical Signals," in *Wavelets in Geophysics*, Efi Foufoula-Georgiou and Praveen Kumar (Eds.), pp. 249–298, Academic Press, San Diego (Ca), 1994.